Energy Storage Materials 63 (2023) 103053

Contents lists available at ScienceDirect

Energy Storage Materials

journal homepage: www.elsevier.com/locate/ensm

Discovery of high entropy garnet solid-state electrolytes via ultrafast synthesis

Yitian Feng [a,1], Lin Yang [a,1], Zihan Yan [b,1], Daxian Zuo [a], Zhewen Zhu [b], Lin Zeng [a], Yizhou Zhu [*,b], Jiayu Wan [*,c]

[a] Department of Mechanical and Energy Engineering, Southern University of Science and Technology, Shenzhen 518055, China
[b] Research Center for Industries of the Future and School of Engineering, Westlake University, Hangzhou 310030, China
[c] Future Battery Research Center, Global Institute of Future Technology, Shanghai Jiaotong University, Shanghai 200240, China

ARTICLE INFO

Keywords:
High-entropy
Garnet
Solid-state electrolyte
Ultrafast synthesis
Materials discovery

ABSTRACT

Multi-elemental functional oxides are crucial for addressing global energy challenges. High entropy oxides (HEO) represent an emerging class of such materials with exceptional performance, attracting significant attention in energy research. However, the concept of high entropy exponentially expands the exploration space of related materials, making the design and discovery of high-performance HEO a challenging task. The synthesis of HEO through a highly efficient and reproducible manner is urgently needed to understand their structure-property relations and develop high-performance materials. In this study, we achieved the ultrafast synthesis of high-entropy garnet $Li_{7+a-c-2d}La_3(A^{3+}{}_aB^{4+}{}_bC^{5+}{}_cD^{6+}{}_d)O_{12}$ (*A*=*Sc*, Y, Bi; *B*=Zr, Mo, Sn, Te, Hf; C=Nb, Sb, Ta; *D*=*W*) in merely tens of seconds. Among the various garnets ranging from unary-garnet to denary-garnet, the quinary-garnet ($Li_{6.6}La_3Zr_{0.4}Sn_{0.4}Sc_{0.4}Ta_{0.4}$-$Nb_{0.4}O_{12}$) exhibits the highest ionic conductivity (3.57×10^{-4} S cm^{-1}) and low electronic conductivity (5.26×10^{-9} S cm^{-1}), with a high critical current density (2.4 mA cm^{-2}) in symmetrical cells. Furthermore, via high-throughput screening of the garnet family, we discover the entropy-stabilization effect, where the synthesized garnet products are gradually stabilized into the desired pure cubic phase with increased configuration entropy. Our work demonstrates a significant step towards the rapid and accurate discovery of high-performance energy materials in the vast multi-elemental material space.

1. Introduction

In facing the world's energy challenges, researchers are dedicated to developing novel energy materials to propel technological advancements [1–3]. Functional energy materials with complicated crystal structures consisting of multiple elements such as $LiNi_{0.8}Co_{0.1}Mn_{0.1}O_2$, [4] $CH(NH_2)_2PbI_3$, [5] and $BaZr_{0.1}Ce_{0.7}Y_{0.1}Yb_{0.1}O_{3-\delta}$ have attracted tremendous research interests due to their unique properties and outstanding performance [6–8]. Among them, oxide material is a particular example in facilitating energy storage technologies, enabling the ubiquitous utilization of Li-ion batteries (LIB) with $LiCoO_2$ and potentially empowering solid state batteries with solid electrolytes ($Li_{6.5}La_3Zr_{1.5}Ta_{0.5}O_{12}$, $Li_{1.3}Al_{0.3}Ti_{1.7}(PO_4)_3$) [9–12]. However, the current energy storage technologies still suffer from the dilemma between energy/power density and safety issues, which can potentially be addressed by improving their key materials [13–15]. Hence, there is an pressing need for the development of suitable materials and corresponding exploratory synthesis methods that allow efficient and accelerated materials discovery for next generation energy storage technologies.

High entropy materials belong to an emerging type of materials that have attracted tremendous research interest in recent decades [16–19]. They were first proposed in 2004 as a means to achieve single phase materials comprising multiple elements [20]. These materials typically contain an equitable mixture of five or more elements, thereby avoiding phase separation by increasing the configuration entropy [21,22]. Originally applied in developing alloys, high entropy materials have demonstrated exceptional strength, ductility, and toughness even at low temperatures, surpassing those of common alloys [23,24]. More recently, high-entropy oxides (HEOs) have made significant advancements due to their unique characteristics such as metastability and lattice distortion, leading to novel properties and functionalities in energy

* Corresponding authors.
E-mail addresses: zhuyizhou@westlake.edu.cn (Y. Zhu), wanjy@sjtu.edu.cn (J. Wan).
[1] These authors contributed equally to this work.

https://doi.org/10.1016/j.ensm.2023.103053
Received 16 September 2023; Received in revised form 6 November 2023; Accepted 7 November 2023
Available online 10 November 2023
2405-8297/© 2023 Elsevier B.V. All rights reserved.

applications [25–27]. For example, in developing oxide solid state electrolytes (SSEs), the high entropy concept enhances the reduction stability of cubic garnet against lithium metal [28], meanwhile introduces lattice distortion that facilitates the ionic conductivity of SSEs [29]. However, discovering high-performance HEOs using traditional "trial-and-error" approaches can be challenging due to the large exploration space resulting from multiple elements [30,31]. Therefore, high-throughput methods that enable the efficient development and design of advanced HEOs are urgently needed for effective screening and identification of their structure-property relationships.

Recently, an emerging class of ultrafast synthesis methods has gained considerable interest due to their unique characteristics, enabling the synthesis of a diverse range of materials, from nano to bulk, within seconds [32–35]. These methods have been proven successful in synthesizing metastable materials, including some high-entropy alloys (HEAs) and HEOs, with relatively simple crystalline structures [36–38]. However, the ultrafast synthesis of high-entropy oxides with complex crystal structures and diverse crystallographic sites remains challenging, primarily due to the potential for detoured reaction pathways and the formation of undesired side products resulting from the intricate combination of precursors, which are currently unexplored to the best of our knowledge [39–41]. To investigate the potential of ultrafast synthesis in creating complex structured high-entropy materials and potentially allow for their accelerated discovery, we employed the ultrafast high-temperature sintering (UHS) technique, studying $Li_7La_3Zr_2O_{12}$ (LLZO) solid state electrolyte as a model system for this research. Cubic phase LLZO offers high ionic conductivity and a wide electrochemical window in contrast to the low performance tetragonal phase [42–45]. Through UHS, we have successfully achieved a rapid synthesis of high-entropy cubic garnets (Zr site high entropy), including quinary-garnet, octonary-garnet, and even denary-garnet. Additionally, we discovered the entropy-stabilization effect, where the augmentation

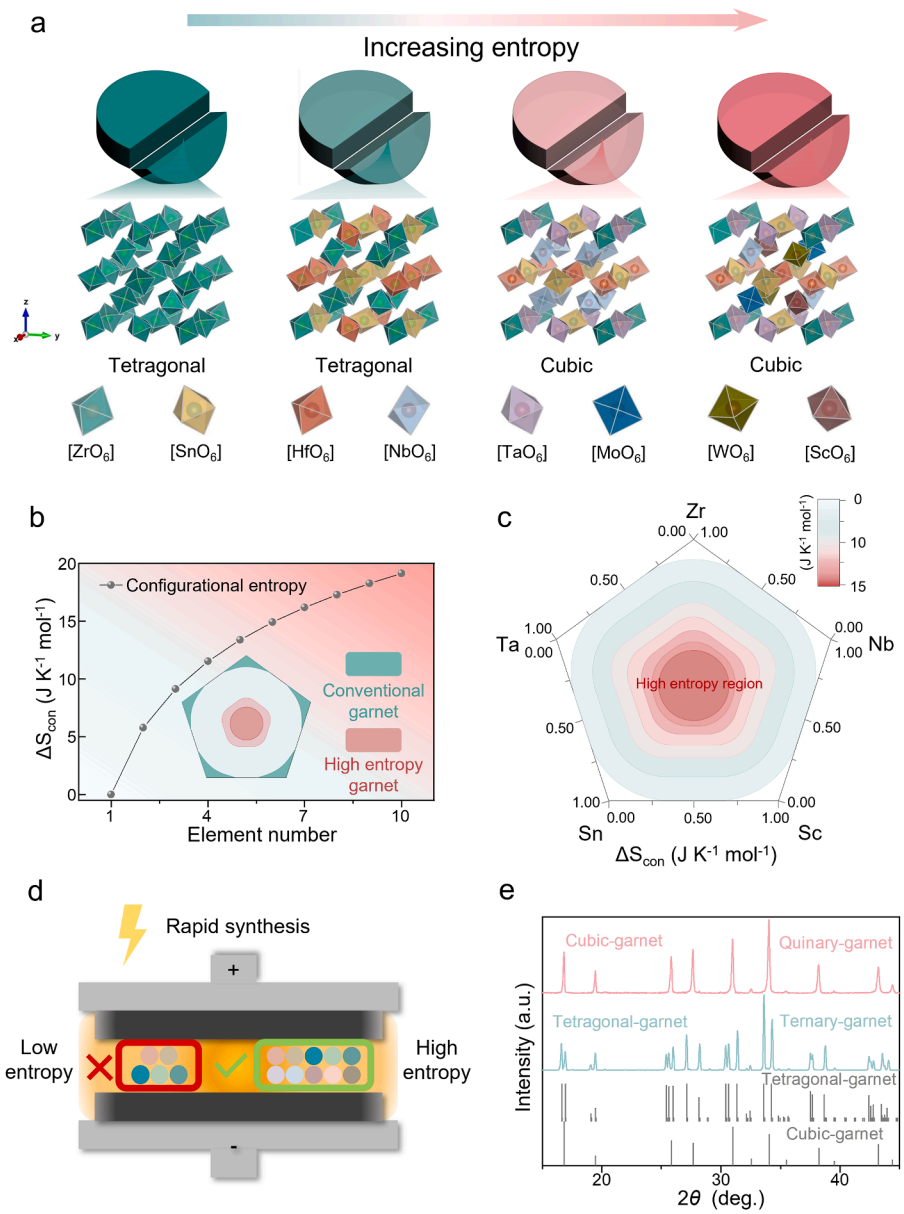

Fig. 1. Concept and schematic of high entropy garnets and their rapid synthesis. (a) Schematic diagram of pellets and lattice structure of garnet from LEGs to HEGs. (b) The change of configurational entropy in garnet with the increase of element number (in the case of equal proportion distribution of each element). (c) Schematic diagram of contour distribution of the mixed configuration entropy of quinary-garnet at different proportions of 5 elements on the Zr site, where the pentagon center represents a situation with an equal proportion of 5 elements, which reaches the maximum mixed configuration entropy (13.83 J K^{-1} mol^{-1}). (d) Schematic diagram of the UHS device and its synthesis of LEGs and HEGs. (e) XRD patterns of as synthesized ternary-garnet and quinary-garnet.

of the configurational entropy can lead to the stabilization of the garnet phase into a pure cubic phase. Among several garnets synthesized ranging from unary-garnet to denary-garnet, the quinary-garnet ($Li_{6.6}La_3Zr_{0.4}Sn_{0.4}Sc_{0.4}Ta_{0.4}Nb_{0.4}O_{12}$) exhibited the highest ionic conductivity (3.57×10^{-4} S cm^{-1}) and low electronic conductivity (5.26×10^{-9} S cm^{-1}), with an impressive critical current density (2.4 mA cm^{-2}). This work showcases an energy- and time-efficient approach for the swift synthesis of high-entropy cubic garnets, demonstrating the possibility of rapid and accurate exploration of high-entropy energy materials with specific target compositions across the wide scope of multi-element materials.

2. Results

To investigate the UHS of high entropy LLZO, we designed and synthesized a series of garnets labeled as $Li_{7+a-c-2d}La_3(A^{3+}{}_aB^{4+}{}_bC^{5+}{}_cD^{6+}{}_d)O_{12}$, where A=Sc, Y, Bi; B=Zr, Mo, Sn, Te, Hf; C=Nb, Sb, Ta; D=W. Fig. 1**a** illustrate the effect of increasing the configurational entropy in the Zr site of garnets to achieve the desired products. We calculate the configuration entropy of LLZO through the formula $\Delta S_{con} = -R\sum_{i=1}^{n} x_i ln x_i$, where R, n, x_i are the gas constant, the total number of elements at the Zr site, and the molar fraction of the ith element, respectively [46]. The calculated configurational entropy rises with an increased number of elements at the Zr site in garnets, ranging from 1 to 10, are shown in Fig. 1**b**. We further calculated the distribution of the configuration entropy of a quinary garnet, as presented in Fig. 1**c**. The mixed configuration entropy increases as the region approaches the center of the pentagon diagram (marked in red). Based on this observation, we postulated that solid solutions containing multiple components, located in the "high-entropy region" at the center of the pentagon diagram, tend to stabilize in the pure cubic phase. It is noteworthy that the low entropy region (indicated by the greenish color) is located near the edge and corner of the diagram, representing conventional doping strategies. In traditional materials development, researchers often focus on the corners of the phase diagram to optimize materials performance [47,48]. However, HEGs occupy most of the garnet space, offering vast opportunities for material exploration and development.

To validate the above speculation and realize rapid synthesis of HEG, we conducted the UHS of ternary-garnet ($Li_7La_3Zr_{0.67}Sn_{0.66}Hf_{0.66}O_{12}$) and quinary-garnet ($Li_{6.6}La_3Zr_{0.4}Sn_{0.4}Sc_{0.4}Ta_{0.4}$-$Nb_{0.4}O_{12}$) with equal molar Zr site elements, as shown in Figs. 1**d, S1** and **S2**. We characterized the crystalline structure of the synthesized products using X-ray diffraction (XRD), as shown in Fig. 1**e**. Our results revealed that the ternary-garnet structure exhibited an undesired tetragonal phase, while the quinary-garnet exhibited an ideal cubic phase. These findings suggest that an increase in configurational entropy can be beneficial in synthesizing desired cubic garnet structures.

To further investigate the impact of configurational entropy on the synthesis of LLZO, we synthesized 5 typical garnets ranging from unary-garnet to denary-garnet, each with equal molar ratio of representative Zr site doping elements, as shown in Fig. 2**a**. We utilized the UHS at approximately 1700 K for a duration of 20 s to synthesize these garnets, and their XRD patterns were presented in Fig. 2**b**. We observed that unary-garnet mainly consisted of tetragonal phase and an impurity phase of $La_2Zr_2O_7$, often observed in garnet synthesis. Meanwhile, the ternary-garnet was primarily tetragonal, and the quinary-garnet, octonary-garnet, and denary-garnet exhibited a desirable cubic phase. Notably, the octonary-garnet and denary-garnet were successfully synthesized and are reported for the first time in the literature to the best of our knowledge. We quantified the phase composition of the synthesized LEGs and HEGs using the Reference Intensity Ratio (RIR) method of Smartlab software, as shown in Fig. 2**c.** Our results indicated that the garnet phase became progressively stabilized towards a pure cubic phase with an increasing number of elements. Specifically, the quinary-garnet, octonary-garnet, and denary-garnet predominantly displayed cubic phases. Thus, our experimental results demonstrate that increasing the configurational entropy guides the gradual stabilization of the garnet phase as it transitions towards a pure cubic phase.

To verify the successful synthesis of elementally uniformly distributed HEGs using UHS technology, we conducted further analysis of

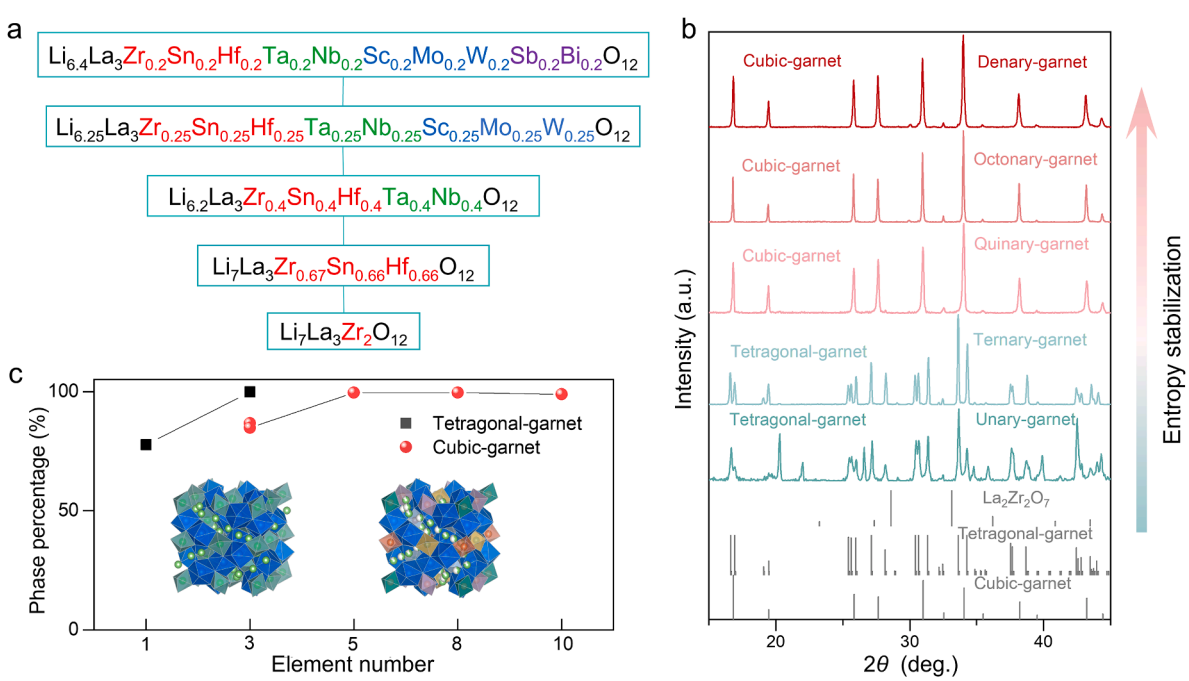

Fig. 2. The discovery of high-entropy-stabilized cubic garnet effect from LEGs to HEGs. (a) UHS of representative unary-garnet, ternary-garnet, quinary-garnet, octonary-garnet, and denary-garnet, along with (b) their corresponding XRD patterns. (c) The XRD phase distribution of a series of garnets from LEGs to HEGs. The phase distribution of unary-garnet is 77.6 % tetragonal phase. Three types of ternary garnets were tested, with one exhibiting a tetragonal phase accounting for 99.85 % of the composition, while the other two exhibited cubic phases accounting for 86.7 % and 84.7 % respectively. In contrast, the quinary-garnet, octonary-garnet and denary-garnet obtain nearly pure cubic phases with proportions of 99.49 %, 99.47 % and 98.79 %, respectively.

HEGs through SEM and TEM characterization. Initially, according to Fig. 3**a**, we observed that HEGs consist of garnet-shaped grains with a size range of approximately 300–500 nm that grow gradually and eventually reach a dense state. This provided preliminary evidence for the successful application of UHS technology to synthesis and sinter HEGs. Subsequently, we confirmed the garnet structure of quinary-garnet ($Li_{6.2}La_3Zr_{0.4}Hf_{0.4}Sn_{0.4}Ta_{0.4}Nb_{0.4}O_{12}$) from the HAADF-STEM image shown in Fig. 3**b**. The FFT image reveals the presence of two crystallographic planes of (321) and (11$\bar{2}$), which correspond to the interplanar spacings of 0.34 and 0.53 nm in the HAADF-STEM image, respectively. Additionally, the uniform distribution of elements in the EDS mapping images confirms that each element is stabilized at the Zr site in quinary-garnet, indicating no element segregation **(Fig. S3)**. Furthermore, Fig. 3**c** and **d** present the EDS mapping result of the octonary-garnet ($Li_{6.25}La_3Zr_{0.25}Hf_{0.25}Sn_{0.25}Sc_{0.25}Ta_{0.25}Nb_{0.25}Mo_{0.25}W_{0.25}O_{12}$) and denary-garnet ($Li_{6.4}La_3Zr_{0.2}Hf_{0.2}Sn_{0.2}Sc_{0.2}Ta_{0.2}Nb_{0.2}Mo_{0.2}Sb_{0.2}W_{0.2}Bi_{0.2}O_{12}$), respectively, demonstrating the homogeneous distribution of each element within the HEGs. These results provide evidence that the elements in HEGs maintain a homogeneous distribution without segregation or aggregation as the number of elements increases. This confirms the successful implementation of UHS technology in synthesizing HEGs and motivates further investigation and experimentation in other energy materials.

To evaluate the performance of HEGs via UHS, we performed both theoretical calculations and electrochemical measurements on LEGs and HEGs (Figs. 4**a and S4**). We calculated the distribution of bond lengths and bond angle of MO_6 octahedral in unary garnet (M = Zr) of quinary garnet (M = Zr, Sn, *Sc*, Ta, Nb) at 300 K. Despite that the bond angle distribution show little difference, the bond length in quinary garnet show wider distribution compared to unary garnet. Such wider bond length distribution indicates that by increasing the number of elements, the local chemical environment in quinary garnet becomes more diverse, which may facilitate faster ionic diffusion **(Figs. S5 and S6)** [29]. We further calculated the probability density of Li ion spatial occupancy unary garnet and quinary garnet under 600 K (Fig. 4**b** and **c**). In quinary garnet, lithium ions show more diffusive behavior within their connected diffusion channels. In comparison, the special distribution of Li ions in unary garnet are more localized. This result is consistent with our electrochemical impedance spectroscopy (EIS) measurement, which the quinary-garnet obtained the lowest impedance as shown in Fig. 4**d**. We compared the Li ion diffusion activation energy between the quinary-garnet and unary-garnet by using both EIS measurements and MD simulations (Fig. 4**e**). Our experiments and simulations showed that the quinary-garnet has a lower activation energy ($E_{a,exp.}$ = 0.36 eV, $E_{a,cal.}$ = 0.30 eV) than the unary-garnet ($E_{a,exp.}$ = 0.45 eV, $E_{a,cal.}$ = 0.47 eV), indicating that high entropy effectively enhances the ion-shuttling property of the garnet SSEs. Another critical parameter affecting the overall performance of garnet SSEs is electronic conductivity. The quinary-garnet SSE exhibits over one order of magnitude reduction in electronic conductivity relative to the unary-garnet, proving that the quinary-garnet SSE can potentially effectively suppress lithium dendrite penetration **(**Fig. 4**f)**. As a result, we assembled LiIn|SSE|LiIn symmetric cells with unary-and quinary-garnet, which their critical current density (CCD) were tested as 0.9 mA cm^{-2} and 2.4 mA cm^{-2}, respectively **(shown in** Fig. 4**g)**. We further performed long-term cycling stability tests on the LiIn|Quinary-garnet|LiIn symmetric cell (Fig. 4**h**), which demonstrate a small overpotential at 0.08 V and stable cycling for 300 h. These results indicate that the quinary-garnet effectively improves the overall performance of garnet SSEs, enhancing their cycling stability and lithium plating/stripping performance.

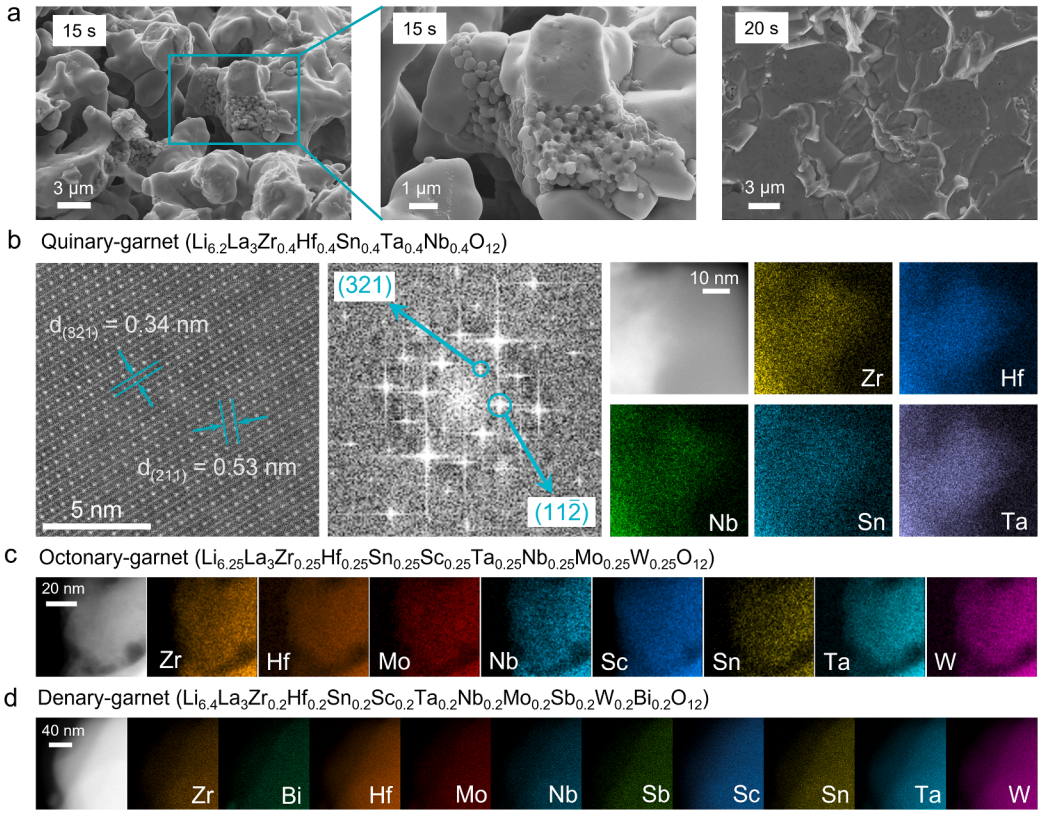

Fig. 3. SEM and TEM microstructural characterization of quinary-garnet, octonary-garnet and denary-garnet. (a) SEM images of HEGs synthesized at 15 s and 20 s via UHS, where the HEG was synthesized into garnet phase at 15 s and into a dense state at 20 s. (b) HAADF-STEM image of quinary-garnet ($Li_{6.2}La_3Zr_{0.4}Hf_{0.4}Sn_{0.4}Ta_{0.4}Nb_{0.4}O_{12}$) and its corresponding fast Fourier transform analysis (FFT) and EDS mapping. (c) EDS mapping of octonary-garnet ($Li_{6.25}La_3Zr_{0.25}Hf_{0.25}Sn_{0.25}Sc_{0.25}Ta_{0.25}Nb_{0.25}Mo_{0.25}W_{0.25}O_{12}$) and (d) denary-garnet ($Li_{6.4}La_3Zr_{0.2}Hf_{0.2}Sn_{0.2}Sc_{0.2}Ta_{0.2}Nb_{0.2}Mo_{0.2}Sb_{0.2}W_{0.2}Bi_{0.2}O_{12}$).

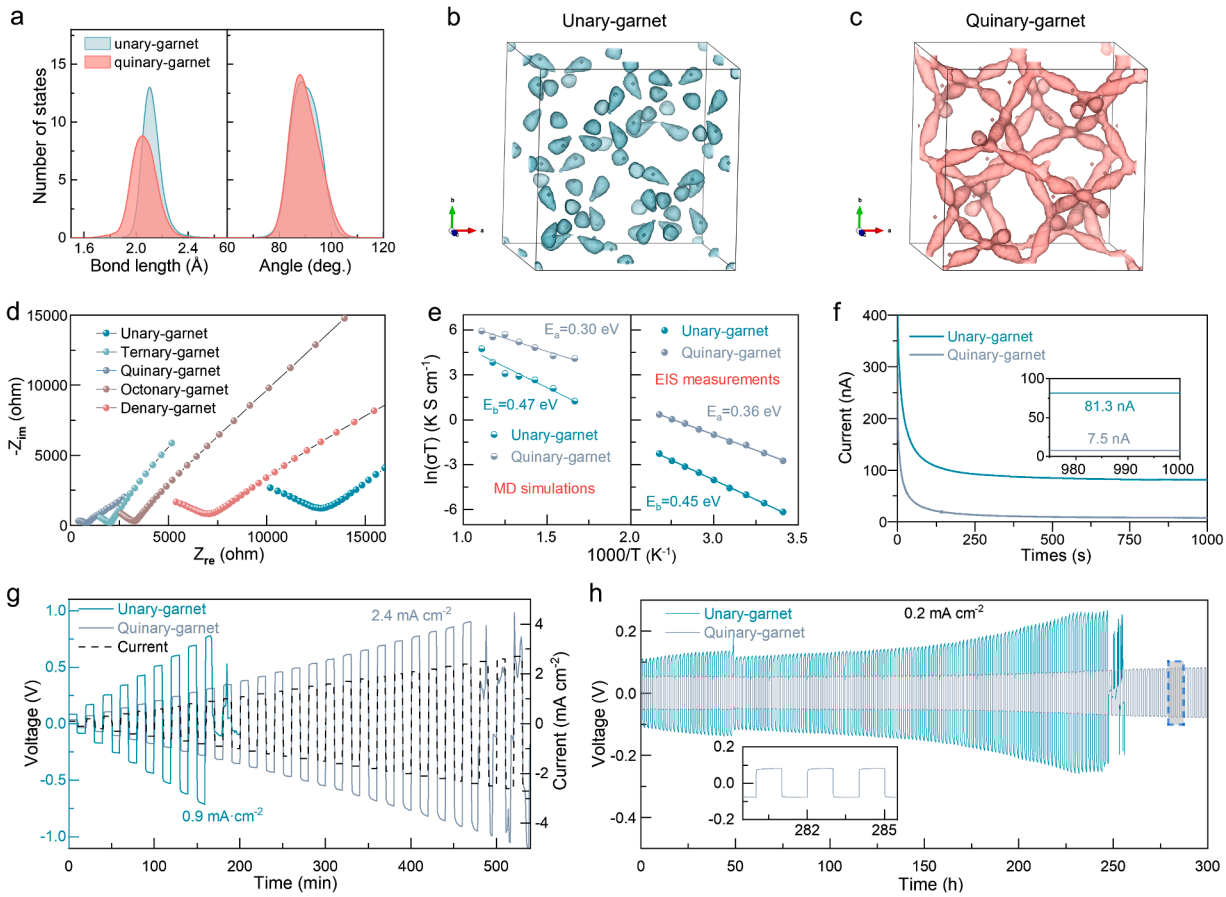

Fig. 4. Electrochemical property comparison of LEGs and HEGs. (a) The statistical distribution of bond lengths (M-O) and bond angles (O-M-O) in unary-garnets and quinary-garnets systems at 300 K. M means the cations that occupy Zr sites (16*c*) as in $Li_7La_3Zr_2O_{12}$ prototype structure. (b, c) The probability density of Li ion spatial occupancy in unary-garnet and quinary-garnet during MD simulations at 600 K. The same simulation parameters and isovalues are set for comparison. (d) EIS results of unary-garnet, ternary-garnet, quinary-garnet, octonary-garnet and denary-garnet. (e) Arrhenius plot of Li ion diffusion in unary-garnet and quinary-garnet SSEs obtained from EIS measurements and MD simulations, respectively, and (f) their corresponding electronic conductivity results. (g) Results of CCD test on LiIn|Unary (Quinary)-garnet|LiIn under conditions of a 0.1 mA cm^{-2} rate increment and a duration of 10 min, and (h) results of constant current cycling test at the current density of 0.2 mA cm^{-2}.

The vast compositional space suggests that HEGs extends beyond what has been presented and synthesized in our experiments. In Fig. 5**a**, we have identified potential candidate elements for HEGs at the Zr site, as highlighted in the periodic table. The availability of multiple options indicates that there is still ample room for further research and development of the high entropy family of garnets. In HEGs, different numbers and types of doping elements can be selected, which allows the tuning of the lithium content, bond length, bond angle, and ion radius (Fig. 5**b**). These parameters can affect the internal characteristics of the material, such as the number of lithium vacancies and lattice distortion. Importantly, as presented in Fig. 5**c**, all of these choices greatly increase the controllability of the electronic conductivity, ionic conductivity, electrochemical stability window, and interface properties of HEGs. Furthermore, the increase in configurational entropy in HEGs leads to an expansion of the solubility limit of elements [46]. The lattice distortion resulting from the mismatch of multiple ion radius sizes, bond lengths, and angles enhances the system's tolerance to elements and promotes the formation of stable phases [26]. Therefore, high entropy design may potentially lead to the design of garnet SSEs and other functional oxides with unprecedented performance in the future.

3. Conclusions

In conclusion, we have successfully employed UHS technology for the rapid synthesis of a series of LEGs and HEGs $Li_{7+a-c-2d}La_3(A_a^{3+}B_b^{4+}C_c^{5+}D^{6+}{}_d)O_{12}$ (*A*=*Sc*, Y, Bi; *B*=Zr, Mo, Sn, Te, Hf; C=Nb, Sb, Ta; *D*=*W*). This approach enables the convenient access to high-performance materials hidden within the exponentially vast high-entropy space, while minimizing energy and time wastage throughout the research and development process. Our results show that from LEGs to HEGs, the garnet phase gradually stabilized in the desired pure cubic phase according to entropy-stabilized garnet effect. The synthesized quinary-garnet ($Li_{6.6}La_3Zr_{0.4}Sn_{0.4}Sc_{0.4}Ta_{0.4}$-$Nb_{0.4}O_{12}$) exhibited an ionic conductivity of 3.57×10^{-4} S cm^{-1} and electronic conductivity of 5.26 $\times 10^{-9}$ S cm^{-1}, as well as significantly increased critical current density of 2.4 mA cm^{-2} and lithium symmetric cycling performance up to 300 h. Despite our success in synthesizing phase-pure octonary-garnet and denary-garnet, their ionic diffusion properties are inferior compared to the quinary-garnet. We believe that our attempts have demonstrated the feasibility of synthesizing HEGs, while the ion combination selection still have a vast potential for further optimization. Further research is need to elucidate the relationship between the ion diffusion mechanism and the composition and structure of HEGs. The high-entropy design strategy can greatly expand the space of exploratory multicomponent materials and provide more possibilities for improving material performance. Our work has paved the way for the rapid and accurate exploration of the exponentially vast high-entropy material space.

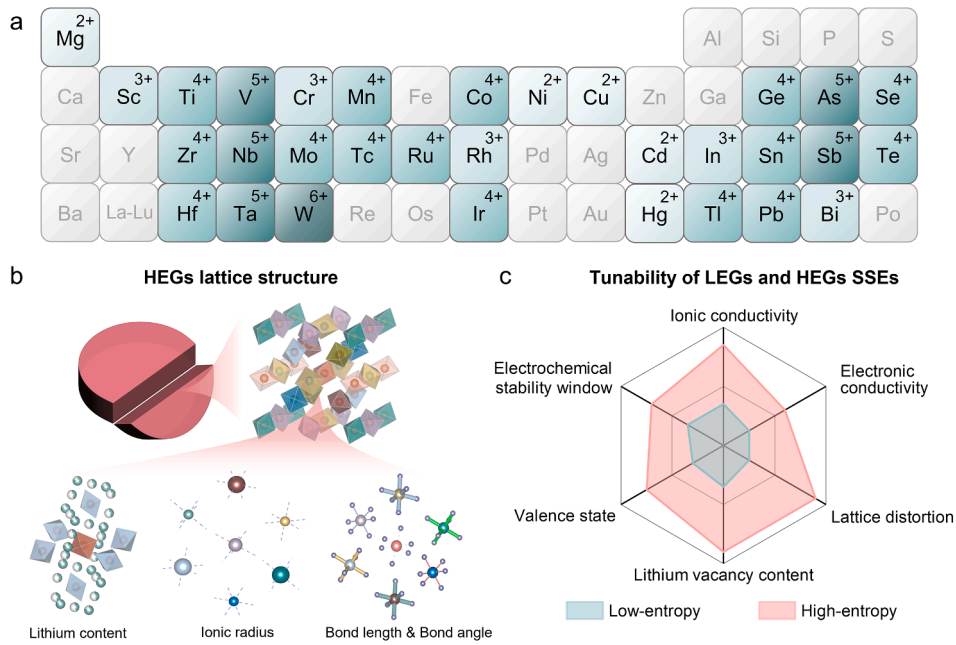

Fig. 5. Schematic images display the vast design space in HEGs. (a) Zr site candidate doping elements in HEGs. The degree of lighting is adjusted according to the valence states of the elements. (b) Schematics of HEGs lattice structures and other detailed information. (c) Comparison of the tunability in various properties of LEGs and HEGs.

4. Methods

4.1. Materials synthesis

The garnet precursor powders were prepared by mixing powders of Li_2CO_3 (99.9 %, Sigma Aldrich), ZrO_2 (99.9 %, Sigma Aldrich), Sc_2O_3/Bi_2O_3/TiO_2/HfO_2/Ta_2O_5/Nb_2O_5/Sb_2O_5/MoO_2/WO_3/SnO_2/TeO_2 (99.9 %, Sigma Aldrich), and La_2O_3 (99.9 %, Sigma Aldrich) powders in a stoichiometric ratio with 10 wt.% excessive Li_2CO_3. The precursor powders were then ball-milled (QM-3SP2-CL) at 600 rpm in isopropyl alcohol for 12 h. After drying overnight at 80 °C, the precursor powders were pressed into pellets (MSK-YLJ-E60T) with a diameter of 10 mm, and then directly synthesized into pellets with the garnet phase via the UHS technique under appropriate conditions. All UHS processes were conducted in an Ar-filled glovebox. The heating rate and temperature of the heater were precisely controlled by tuning the current and voltage of the direct current (DC) power (StarPower, 1500 W). The heating rate was approximately 200 K s^{-1}, reaching 1700 K within 7 s, maintaining that temperature for 13 s, sintering for a total of 20 s, and then cooling naturally. The temperature of the heater was calculated from the UV–Vis spectra measured with a Vision Research Phantom Miro M110 high-speed camera with an error bar of about ± 100 °C.

For garnet SSEs, firstly, the garnet pellets were ground, then milled with 600 rpm in isopropanol for 12 h, and then dried overnight at 80 °C. The dried powder was then sintered in a box furnace at 1200 °C for 12 h. Garnet SSEs pellets were polished with 1000 mesh, 2000 mesh and 5000 mesh sandpaper and stored in a glove box for electrochemical testing.

4.2. Materials characterizations

X-ray diffraction (XRD) patterns of samples were collected using a MiniFlex 600 X-ray diffractometer with Cu Kα radiation (40 kV, 15 mA) and a 2θ ranging from 10° to 60° Smartlab software was used for the peak fitting of XRD data, and the fitting function of diffraction peak shape is Pseudo-Voigt Function. And then Reference Intensity Ratio (RIR) method was used for quantitative analysis of various phase contents of samples by powder diffraction analysis. The formula for the RIR method is shown in Eq. (1).

$$W_a = \frac{I_a^{max}}{RIR_a} \times \left(\sum_1^n \frac{I_k}{RIR_k} \right)^{-1} \quad (1)$$

where, W_a is the phase content, I_a^{max} is the area of the strongest peak, and RIR is the value of RIR corresponding to the phase.

Scanning electron microscope (SEM) images were obtained using a Sigma 300 field emission SEM instrument with energy-dispersive X-ray spectroscopy (EDS). For the transmission electron microscopy (TEM) investigation, the samples were thoroughly ground into powders and diluted in ethanol by ultrasonic treatment for 5 min. The suspension liquid was dripped onto holey carbon-coated Cu grids. The high-resolution transmission electron microscopy (HRTEM), high-angle annular dark-field scanning transmission electron microscopy (HAADF-STEM), and energy dispersive spectroscopy (EDS) experiments were performed using an FEI Talos F200X G2 microscope at an accelerating voltage of 200 KV.

4.3. Electrochemical measurements

Ionic conductivity was measured using AC impedance analysis (BioLogic VMP3 potentiostat). The frequency applied ranged from 7 MHz to 1 Hz with an amplitude of 10 mV. A thin layer of Pt was sputtered on each surface of the pellets as blocking electrodes. Ionic conductivity was calculated based on the following Equation: $\sigma_t = \frac{L}{R_t S}$, where σ_t, L, S, and R_t represent the ionic conductivity, thickness of electrolyte pellets, electrolyte pellet surface area, and resistance value. Activation energies were calculated from the slope of the resulting Arrhenius plot. Electronic conductivity was examined by DC polarization experiment with a DC voltage of 0.1 V, and Pt was also sputtered on both sides of the pellets. Galvanostatic stripping-plating of the LiIn|garnet SSEs|LiIn symmetric cells was recorded at room temperature with a current density of 0.2 mA cm^{-2}. Lithium indium alloy was ultrasonically attached on the surface of the solid electrolyte pellet using an ultrasonic household cleaner [49]. The solid electrolyte's critical current density (CCD) was evaluated by assembling LiIn|garnet SSEs|LiIn symmetric cell using an automatic battery tester system (Neware Technology Limited) at room temperature, which was tested by rate cycling

under an initial current density of 0.1 mA cm^{-2} with an increasing step of 0.1 mA cm^{-2}. In addition, full cell of $LiFePO_4$//quinary-garnet//Li was assembled and tested, as shown in **(Fig. S7)** [28,50].

4.4. Theoretical calculations

We trained Moment Tensor Potentials (MTPs) [51], which is a machine-learning based classical interatomic potentials using the MLIP package [52]. The unary-garnets system (including 56 Li, 24 La, 16 Zr, and 96 O) and quinary-garnets system (including 52 Li, 24 La, 3 Zr, 3 Sn, 4 Ta, 3 Nb, 3 Sn, 96 O) were used in all trainings and MD simulations. The initial structure of the quinary-garnets system was constructed by using the special quasi-random structure (SQS) configuration implemented in the ICET code [53,54].

We performed AIMD simulations to generate the initial training set. All DFT calculation were performed using the Vienna *Ab initio* Simulation Package (VASP) [55,56]. Projector-augmented wave (PAW) method was used to describe the electron-ion interaction with the plane-wave energy cutoff of 520 eV [57]. The exchange-correlation energy was described by the generalized gradient approximation (GGA) with the revised Perdew-Burke-Ernzerhof for solids (PBEsol) exchange functional [58,59]. The *k*-point mesh was $1 \times 1 \times 1$ and the convergence accuracy for energy and force were 10^{-5} eV and 0.01 eV/Å, respectively.

We used the active learning strategy to iteratively expand the training set. The functional form of MTP of level 10 and the cutoff distance of 12 Å were set. Finally, 631 and 868 configurations were selected to construct the MTPs for unary and quinary garnet system, respectively. The root-mean square errors of energy, force and stress were 0.89 meV/atom, 66.12 meV/Å and 0.11 GPa for unary-garnet, while 0.94 meV/atom, 81.94 meV/Å and 0.14 GPa for quinary-garnet, respectively.

LAMMPS package was employed to perform the molecular dynamics (MD) simulations. The lattice parameters of unary-garnets and quinary-garnets systems at different temperatures can be obtained by performing 100 ps MD simulations using the Nosé-Hoover barostat and thermostat method (NPT) with the timesteps of 1 fs. After that, MD simulations for ion diffusion were performed using NVT method with the corresponding lattice parameters for a total of 0.5–10 ns until the ionic conductivity was converged (the total mean square displacement (TMSD) > 2500 $Å^2$). The diffusivity of Li ion was calculated as the mean square displacement over time interval as in previous works [60,61]. We also employed pymatgen, VESTA and OVITO packages for data processing and graphics production [62–64].

CRediT authorship contribution statement

Yitian Feng: Conceptualization, Methodology, Validation, Investigation, Writing – original draft. **Lin Yang:** Conceptualization, Investigation, Writing – original draft. **Zihan Yan:** Software, Investigation, Writing – original draft. **Daxian Zuo:** Visualization, Writing – review & editing. **Zhewen Zhu:** Visualization, Investigation, Software. **Lin Zeng:** Writing – review & editing. **Yizhou Zhu:** Software, Validation, Visualization, Supervision, Writing – review & editing. **Jiayu Wan:** Conceptualization, Funding acquisition, Project administration, Supervision, Writing – review & editing.

Declaration of Competing Interest

The authors declare that they have no known competing financial interests or personal relationships that could have appeared to influence the work reported in this paper.

Acknowledgements

We would like to acknowledge funding support from National Natural Science Foundation of China 52272215 and the Research Center for industries of the Future (RCIF) at Westlake University and the start-up fund from Westlake University.

Supplementary materials

Supplementary material associated with this article can be found, in the online version, at doi:10.1016/j.ensm.2023.103053.

References

[1] C. Wang, W. Ping, Q. Bai, H. Cui, R. Hensleigh, R. Wang, A.H. Brozena, Z. Xu, J. Dai, Y.J.S. Pei, A general method to synthesize and sinter bulk ceramics in seconds, Science 368 (2020) 521–526, https://doi.org/10.1126/science.aaz7681.
[2] G. Ji, J. Wang, Z. Liang, K. Jia, J. Ma, Z. Zhuang, G. Zhou, H.M. Cheng, Direct regeneration of degraded lithium-ion battery cathodes with a multifunctional organic lithium salt, Nat. Commun. 14 (2023) 584, https://doi.org/10.1038/s41467-023-36197-6.
[3] G. Zhou, H. Chen, Y. Cui, Formulating energy density for designing practical lithium–sulfur batteries, Nat. Energy 7 (2022) 312–319, https://doi.org/10.1038/s41560-022-01001-0.
[4] P. Xiao, Y. Zhao, Z. Piao, B. Li, G. Zhou, H.M. Cheng, A nonflammable electrolyte for ultrahigh-voltage (4.8V-class) Li||NCM811 cells with a wide temperature range of 100°C, Energy Environ. Sci. 15 (2022) 2435–2444, https://doi.org/10.1039/d1ee02959b.
[5] W. Hui, L. Chao, H. Lu, F. Xia, Q. Wei, Z. Su, T. Niu, L. Tao, B. Du, D.J.S. Li, Stabilizing black-phase formamidinium perovskite formation at room temperature and high humidity, Science 371 (2021) 1359–1364, https://doi.org/10.1126/science.abf7652.
[6] W. Bian, W. Wu, B. Wang, W. Tang, M. Zhou, C. Jin, H. Ding, W. Fan, Y. Dong, J. Li, D. Ding, Revitalizing interface in protonic ceramic cells by acid etch, Nature 604 (2022) 479–485, https://doi.org/10.1038/s41586-022-04457-y.
[7] D. Zuo, L. Yang, Z. Zou, S. Li, Y. Feng, S.J. Harris, S. Shi, J. Wan, Ultrafast synthesis of nasicon solid electrolytes for sodium-metal batteries, Adv. Energy Mater. (2023), 2301540, https://doi.org/10.1002/aenm.202301540.
[8] F. Ding, C. Zhao, D. Zhou, Q. Meng, D. Xiao, Q. Zhang, Y. Niu, Y. Li, X. Rong, Y. Lu, L. Chen, Y.S. Hu, A novel Ni-rich O_3-$Na[Ni_{0.60}Fe_{0.25}Mn_{0.15}]O_2$ cathode for Na-ion batteries, Energy Storage Mater. 30 (2020) 420–430, https://doi.org/10.1016/j.ensm.2020.05.013.
[9] J. Wang, K. Jia, J. Ma, Z. Liang, Z. Zhuang, Y. Zhao, B. Li, G. Zhou, H.M. Cheng, Sustainable upcycling of spent $LiCoO_2$ to an ultra-stable battery cathode at high voltage, Nat. Sustain. 6 (2023) 797–805, https://doi.org/10.1038/s41893-023-01094-9.
[10] J.N. Zhang, Q. Li, C. Ouyang, X. Yu, M. Ge, X. Huang, E. Hu, C. Ma, S. Li, R. Xiao, W. Yang, Y. Chu, Y. Liu, H. Yu, X.Q. Yang, X. Huang, L. Chen, H. Li, Trace doping of multiple elements enables stable battery cycling of $LiCoO_2$ at 4.6 V, Nat. Energy 4 (2019) 594–603, https://doi.org/10.1038/s41560-019-0409-z.
[11] Z. Jin, X. Kong, H. Huang, Y. Jiang, W. Xiang, Y. Xu, L. Zhang, R. Peng, C. Wang, Garnet-type solid-state mixed ionic and electronic conductor, Energy Storage Mater. 59 (2023), 102788, https://doi.org/10.1016/j.ensm.2023.102788.
[12] J. Zhu, Y. Xiang, J. Zhao, H. Wang, Y. Li, B. Zheng, H. He, Z. Zhang, J. Huang, Y. Yang, Insights into the local structure, microstructure and ionic conductivity of silicon doped NASICON-type solid electrolyte $Li_{1.3}Al_{0.3}Ti_{1.7}P_3O_{12}$, Energy Storage Mater. 44 (2022) 190–196, https://doi.org/10.1016/j.ensm.2021.10.003.
[13] R. Chen, Q. Li, X. Yu, L. Chen, H. Li, Approaching practically accessible solid-state batteries: stability issues related to solid electrolytes and interfaces, Chem. Rev. 120 (2020) 6820–6877, https://doi.org/10.1021/acs.chemrev.9b00268.
[14] Y. Guo, S. Wu, Y.B. He, F. Kang, L. Chen, H. Li, Q.H. Yang, Solid-state lithium batteries: safety and prospects, eScience 2 (2022) 138–163, https://doi.org/10.1016/j.esci.2022.02.008.
[15] Q. Zhao, S. Stalin, C.Z. Zhao, L.A. Archer, Designing solid-state electrolytes for safe, energy-dense batteries, Nat. Rev. Mater. 5 (2020) 229–252, https://doi.org/10.1038/s41578-019-0165-5.
[16] F. Ding, C. Zhao, D. Xiao, X. Rong, H. Wang, Y. Li, Y. Yang, Y. Lu, Y.S. Hu, Using high-entropy configuration strategy to design Na-ion layered oxide cathodes with superior electrochemical performance and thermal stability, J. Am. Chem. Soc. 144 (2022) 8286–8295, https://doi.org/10.1021/jacs.2c02353.
[17] Y. Su, X. Rong, H. Li, X. Huang, L. Chen, B. Liu, Y.S. Hu, High-entropy microdomain interlocking polymer electrolytes for advanced all-solid-state battery chemistries, Adv. Mater. 35 (2023), e2209402, https://doi.org/10.1002/adma.202209402.
[18] C. Zhao, F. Ding, Y. Lu, L. Chen, Y.S. Hu, High-entropy layered oxide cathodes for sodium-ion batteries, Angew. Chem. Int. Ed. 59 (2020) 264–269, https://doi.org/10.1002/anie.201912171.
[19] Y.F. Ye, Q. Wang, J. Lu, C.T. Liu, Y. Yang, High-entropy alloy: challenges and prospects, Mater. Today 19 (2016) 349–362, https://doi.org/10.1016/j.mattod.2015.11.026.
[20] J.W. Yeh, S.K. Chen, S.J. Lin, J.Y. Gan, T.S. Chin, T.T. Shun, C.H. Tsau, S.Y. Chang, Nanostructured high-entropy alloys with multiple principal elements: novel alloy design concepts and outcomes, Adv. Eng. Mater. 6 (2004) 299–303, https://doi.org/10.1002/adem.200300567.
[21] A. Sarkar, Q. Wang, A. Schiele, M.R. Chellali, S.S. Bhattacharya, D. Wang, T. Brezesinski, H. Hahn, L. Velasco, B. Breitung, High-entropy oxides: fundamental aspects and electrochemical properties, Adv. Mater. 31 (2019), e1806236, https://doi.org/10.1002/adma.201806236.

[22] N. Dragoe, D.J.S. Bérardan, Order emerging from disorder, Science 366 (2019) 573–574, https://doi.org/10.1126/science.aaz1598.
[23] O.M. Smith, G. Riddihough, M.M. Moerchen, M.S. Lavine, N.S. Wigginton, L. M. Zahn, S.M. Hurtley, L.K. Ferrarelli, P.A. Kiberstis, P. Szuromi, H.J. Smith, J. Stajic, A metal alloy that is stronger when cold, Science 345 (2014), https://doi.org/10.1126/science.2014.345.6201.twis, 1131-1131.
[24] K.M. Youssef, A.J. Zaddach, C. Niu, D.L. Irving, C.C. Koch, A novel low-density, high-hardness, high-entropy alloy with close-packed single-phase nanocrystalline structures, Mater. Res. Lett. 3 (2014) 95–99, https://doi.org/10.1080/21663831.2014.985855.
[25] C. Oses, C. Toher, S. Curtarolo, High-entropy ceramics, Nat. Rev. Mater. 5 (2020) 295–309, https://doi.org/10.1038/s41578-019-0170-8.
[26] C.M. Rost, E. Sachet, T. Borman, A. Moballegh, E.C. Dickey, D. Hou, J.L. Jones, S. Curtarolo, J.P. Maria, Entropy-stabilized oxides, Nat. Commun. 6 (2015) 8485, https://doi.org/10.1038/ncomms9485.
[27] M. Botros, J.J.S. Janek, Embracing disorder in solid-state batteries, Science 378 (2022) 1273–1274, https://doi.org/10.1126/science.adf3383.
[28] S.K. Jung, H. Gwon, H. Kim, G. Yoon, D. Shin, J. Hong, C. Jung, J.S. Kim, Unlocking the hidden chemical space in cubic-phase garnet solid electrolyte for efficient quasi-all-solid-state lithium batteries, Nat. Commun. 13 (2022) 7638, https://doi.org/10.1038/s41467-022-35287-1.
[29] Y. Zeng, B. Ouyang, J. Liu, Y.W. Byeon, Z. Cai, L.J. Miara, Y. Wang, G.J.S. Ceder, High-entropy mechanism to boost ionic conductivity, Science 378 (2022) 1320–1324, https://doi.org/10.1126/science.abq1346.
[30] B. Ouyang, J. Wang, T. He, C.J. Bartel, H. Huo, Y. Wang, V. Lacivita, H. Kim, G. Ceder, Synthetic accessibility and stability rules of NASICONs, Nat. Commun. 12 (2021) 5752, https://doi.org/10.1038/s41467-021-26006-3.
[31] Z. Wang, X. Lin, Y. Han, J. Cai, S. Wu, X. Yu, J. Li, Harnessing artificial intelligence to holistic design and identification for solid electrolytes, Nano Energy 89 (2021), 106337, https://doi.org/10.1016/j.nanoen.2021.106337.
[32] M. Cui, C. Yang, S. Hwang, M. Yang, S. Overa, Q. Dong, Y. Yao, A.H. Brozena, D. A. Cullen, M.J.S. Chi, Multi-principal elemental intermetallic nanoparticles synthesized via a disorder-to-order transition, Sci. Adv. 8 (2022) eabm4322, https://doi.org/10.1126/sciadv.abm4322.
[33] M. Hong, Q. Dong, H. Xie, B.C. Clifford, J. Qian, X. Wang, J. Luo, L. Hu, Ultrafast sintering of solid-state electrolytes with volatile fillers, ACS Energy Lett. 6 (2021) 3753–3760, https://doi.org/10.1021/acsenergylett.1c01554.
[34] X. Hu, D. Zuo, S. Cheng, S. Chen, Y. Liu, W. Bao, S. Deng, S.J. Harris, J. Wan, Ultrafast materials synthesis and manufacturing techniques for emerging energy and environmental applications, Chem. Soc. Rev. 52 (2023) 1103–1128, https://doi.org/10.1039/d2cs00322h.
[35] W. Ping, C. Wang, R. Wang, Q. Dong, Z. Lin, A.H. Brozena, J. Dai, J. Luo, L.J.S. A. Hu, Printable, high-performance solid-state electrolyte films, Sci. Adv. 6 (2020) eabc8641, https://doi.org/10.1126/sciadv.abc8641.
[36] L. Spiridigliozzi, G. Dell'Agli, S. Esposito, P. Rivolo, S. Grasso, V.M. Sglavo, M. Biesuz, Ultra-fast high-temperature sintering (UHS) of $Ce_{0.2}Zr_{0.2}Y_{0.2}Gd_{0.2}La_{0.2}O_{2-\delta}$ fluorite-structured entropy-stabilized oxide (F-ESO), Scr. Mater. 214 (2022), 114655, https://doi.org/10.1016/j.scriptamat.2022.114655.
[37] C. Wang, W. Zhong, W. Ping, Z. Lin, R. Wang, J. Dai, M. Guo, W. Xiong, J.C. Zhao, L. Hu, Rapid synthesis and sintering of metals from powders, Adv. Sci. 8 (2021), e2004229, https://doi.org/10.1002/advs.202004229.
[38] Y. Yao, Q. Dong, A. Brozena, J. Luo, J. Miao, M. Chi, C. Wang, I.G. Kevrekidis, Z. J. Ren, J. Greeley, G. Wang, A. Anapolsky, L. Hu, High-entropy nanoparticles: synthesis-structure-property relationships and data-driven discovery, Science 376 (2022) eabn3103, https://doi.org/10.1126/science.abn3103.
[39] Z. Lun, B. Ouyang, D.H. Kwon, Y. Ha, E.E. Foley, T.Y. Huang, Z. Cai, H. Kim, M. Balasubramanian, Y. Sun, J. Huang, Y. Tian, H. Kim, B.D. McCloskey, W. Yang, R.J. Clement, H. Ji, G. Ceder, Cation-disordered rocksalt-type high-entropy cathodes for Li-ion batteries, Nat. Mater. 20 (2021) 214–221, https://doi.org/10.1038/s41563-020-00816-0.
[40] K. Jun, Y. Sun, Y. Xiao, Y. Zeng, R. Kim, H. Kim, L.J. Miara, D. Im, Y. Wang, G. Ceder, Lithium superionic conductors with corner-sharing frameworks, Nat. Mater. 21 (2022) 924–931, https://doi.org/10.1038/s41563-022-01222-4.
[41] Y. Xiao, K. Jun, Y. Wang, L.J. Miara, Q. Tu, G. Ceder, Lithium oxide superionic conductors inspired by garnet and NASICON structures, Adv. Energy Mater. 11 (2021), 2101437, https://doi.org/10.1002/aenm.202101437.
[42] Y. Li, C.A. Wang, H. Xie, J. Cheng, J.B. Goodenough, High lithium ion conduction in garnet-type $Li_6La_3ZrTaO_{12}$, Electrochem. Commun. 13 (2011) 1289–1292, https://doi.org/10.1016/j.elecom.2011.07.008.
[43] H. Xie, J.A. Alonso, Y. Li, M.T. Fernández-Díaz, J.B. Goodenough, Lithium distribution in aluminum-free cubic $Li_7La_3Zr_2O_{12}$, Chem. Mater. 23 (2011) 3587–3589, https://doi.org/10.1021/cm201671k.
[44] C. Wang, K. Fu, S.P. Kammampata, D.W. McOwen, A.J. Samson, L. Zhang, G. T. Hitz, A.M. Nolan, E.D. Wachsman, Y. Mo, V. Thangadurai, L. Hu, Garnet-type solid-state electrolytes: materials, interfaces, and batteries, Chem. Rev. 120 (2020) 4257–4300, https://doi.org/10.1021/acs.chemrev.9b00427.
[45] Y. Wang, Y. Wu, Z. Wang, L. Chen, H. Li, F. Wu, Doping strategy and mechanism for oxide and sulfide solid electrolytes with high ionic conductivity, J. Mater. Chem. A 10 (2022) 4517–4532, https://doi.org/10.1039/d1ta10966a.
[46] B. Jiang, Y. Yu, J. Cui, X. Liu, L. Xie, J. Liao, Q. Zhang, Y. Huang, S. Ning, B.J.S. Jia, High-entropy-stabilized chalcogenides with high thermoelectric performance, Science 371 (2021) 830–834, https://doi.org/10.1126/science.abe1292.
[47] H. Xie, Y. Li, J. Han, Y. Dong, M.P. Paranthaman, L. Wang, M. Xu, A. Gupta, Z. Bi, C.A. Bridges, M. Nakanishi, A.P. Sokolov, J.B. Goodenough, $Li_6La_3SnMO_{12}$(M = Sb, Nb, Ta), a family of lithium garnets with high Li-ion conductivity, J. Electrochem. Soc 159 (2012) A1148–A1151, https://doi.org/10.1149/2.009208jes.
[48] S. Kim, J.S. Kim, L. Miara, Y. Wang, S.K. Jung, S.Y. Park, Z. Song, H. Kim, M. Badding, J. Chang, V. Roev, G. Yoon, R. Kim, J.H. Kim, K. Yoon, D. Im, K. Kang, High-energy and durable lithium metal batteries using garnet-type solid electrolytes with tailored lithium-metal compatibility, Nat. Commun. 13 (2022) 1883, https://doi.org/10.1038/s41467-022-29531-x.
[49] X. Wang, J. Chen, D. Wang, Z. Mao, Improving the alkali metal electrode/inorganic solid electrolyte contact via room-temperature ultrasound solid welding, Nat. Commun. 12 (2021) 7109, https://doi.org/10.1038/s41467-021-27473-4.
[50] S.A. Pervez, P. Ganjeh-Anzabi, U. Farooq, M. Trifkovic, E.P.L. Roberts, V. Thangadurai, Fabrication of a dendrite-free all solid-state li metal battery via polymer composite/garnet/polymer composite layered electrolyte, Adv. Mater. Interfaces 6 (2019), 1900186, https://doi.org/10.1002/admi.201900186.
[51] A.V. Shapeev, Moment tensor potentials: a class of systematically improvable interatomic potentials, Multiscale Model. Simul. 14 (2016) 1153–1173, https://doi.org/10.1137/15m1054183.
[52] I.S. Novikov, K. Gubaev, E.V. Podryabinkin, A.V. Shapeev, The MLIP package: moment tensor potentials with MPI and active learning, Mach. Learn. Sci. Technol. 2 (2021), 025002, https://doi.org/10.1088/2632-2153/abc9fe.
[53] A. Zunger, S. Wei, L.G. Ferreira, J.E. Bernard, Special quasirandom structures, Phys. Rev. Lett. 65 (1990) 353–356, https://doi.org/10.1103/PhysRevLett.65.353.
[54] M. Ångqvist, W.A. Muñoz, J.M. Rahm, E. Fransson, C. Durniak, P. Rozyczko, T. H. Rod, P. Erhart, ICET – a python library for constructing and sampling alloy cluster expansions, Adv. Theory Simul. 2 (2019), 1900015, https://doi.org/10.1002/adts.201900015.
[55] A. Notario-Estevez, S.M. Kozlov, F. Vines, F. Illas, Electronic-structure-based material descriptors: (in)dependence on self-interaction and Hartree-Fock exchange, Phys. Rev. B 51 (2015) 5602–5605, https://doi.org/10.1039/c4cc10427g.
[56] L.M. Ramaniah, C. Kamal, S.J.P.R.B. Sikka, First principles DFT study of weak CH… O bonds in crystalline amino acids under pressure-alanine, Phys. Rev. B 49 (1994) 14251–14269, https://doi.org/10.1063/1.4790935.
[57] P.E. Blochl, Projector augmented-wave method, Phys. Rev. B 50 (1994) 17953–17979, https://doi.org/10.1103/physrevb.50.17953.
[58] J.P. Perdew, K. Burke, M. Ernzerhof, Generalized gradient approximation made simple, Phys. Rev. Lett. 77 (1996) 3865–3868, https://doi.org/10.1103/PhysRevLett.77.3865.
[59] J.P. Perdew, A. Ruzsinszky, G.I. Csonka, O.A. Vydrov, G.E. Scuseria, L. A. Constantin, X. Zhou, K. Burke, Erratum: restoring the density-gradient expansion for exchange in solids and surfaces [Phys. Rev. Lett.100, 136406 (2008)], Phys. Rev. Lett. 102 (2009), 039902, https://doi.org/10.1103/PhysRevLett.102.039902.
[60] X. He, Q. Bai, Y. Liu, A.M. Nolan, C. Ling, Y. Mo, Crystal structural framework of lithium super-ionic conductors, Adv. Energy Mater. 9 (2019), 1902078, https://doi.org/10.1002/aenm.201902078.
[61] S. Wang, Y. Liu, Y. Mo, Frustration in super-ionic conductors unraveled by the density of atomistic states, Angew. Chem. Int. Ed. 62 (2023), e202215544, https://doi.org/10.1002/anie.202215544.
[62] Y. Mo, S.P. Ong, G. Ceder, First principles study of the $Li_{10}GeP_2S_{12}$ lithium super ionic conductor material, Chem. Mater. 24 (2011) 15–17, https://doi.org/10.1021/cm203303y.
[63] K. Momma, F.J.J.O.A.C. Izumi, VESTA 3 for three-dimensional visualization of crystal, volumetric and morphology data, J. Appl. Crystallogr. 44 (2011) 1272–1276, https://doi.org/10.1107/S0021889811038970.
[64] A. Stukowski, Visualization and analysis of atomistic simulation data with OVITO–the open visualization tool, Model. Simul. Mater. Sci. Eng. 18 (2010), 015012, https://doi.org/10.1088/0965-0393/18/1/015012.